Available online at www.sciencedirect.com
SCIENCE DIRECT®
International Journal of Heat and Fluid Flow 26 (2005) 12–24
International Journal of HEAT AND FLUID FLOW
www.elsevier.com/locate/ijhff

Airflow characteristics within a slot-ventilated enclosure

J. Moureh [a,b,*], D. Flick [a,c]

[a] UMR Génie Industriel Alimentaire Cemagref-ENSIA-INAPG-INRA, France
[b] Refrigerating Process Engineering Unit, Parc de Tourvoie, Cemagref-BP 44, 92163 Antony Cedex, France
[c] INA-PG 16, rue Claude Bernard, 75005 Paris, France

Received 20 June 2003; accepted 6 May 2004
Available online 16 September 2004

Abstract

The objective of this study is to numerically and experimentally investigate velocity characteristics throughout a long slot-ventilated enclosure as a function of inlet flow arrangement located on the same side of the exit section. This study focused on the effect of the enclosure's confinement on the airflow pattern and more particularly on the wall jet characteristics concerning its decay and its stabilisation. An original approach is also proposed to evaluate the local effect of airflow pattern on ventilation efficiency. To improve the performance and the uniformity of ventilation in the enclosure, a new configuration with a lateral air inlet section was studied. The results concerning airflow characteristics and air-ventilation efficiency were compared and contrasted with the more common case with a central inlet section. A numerical approach based on computational fluid dynamics (CFD) Fluent code was used to test various turbulence closure models including the high and low Reynolds number form of the two-equation k–ε model and the more advanced Reynolds stress model (RSM). Comparisons with experimental data obtained on a scale model under isothermal conditions allow a critical evaluation of the performance of these models in internal flows.

Keywords: Airflow; CFD; Numerical modelling; Enclosure; Wall jet; Ventilation

1. Introduction

Within slot-ventilated enclosures extensively used in many engineering applications, airflow patterns and velocity characteristics are very important to regulate and control the level and the homogeneity of indoor ambience parameters such as temperature, humidity and contaminant concentration. This is particularly important from the viewpoint of air quality, thermal comfort, health and energy savings.

Many studies have been performed in order to characterize experimentally and/or numerically the influence of aerodynamic and geometric parameters related to the inlet jet, the enclosure's dimensions and the positions of the inlet and the outlet sections on airflow patterns and ventilation efficiency (Yu and Hoff, 1999; Karimipanah, 1999; Adre and Albright's, 1994; Zhang et al., 2000; Awbi, 1989; Nielsen et al., 1978; Davidson, 1989; Hoff et al., 1992; Choi et al., 1990; Nady et al., 1995).

In most configurations investigated (Awbi, 1989, Nielsen et al., 1978; Davidson, 1989; Hoff et al., 1992; Choi et al., 1990; Nady et al., 1995), the inlet and outlet are located face to face in order to promote a robust airflow in the whole internal space. This paper focuses the particular case of an empty slot-ventilated room with inlet and outlet sections located on the same side. From an aerodynamic standpoint, the principal drawback of this design is the presence of a strong pathway between the two sections, implying high velocities in the front section and low velocities in the rear part of the enclosure. Concerning this type of configuration, the investigations

* Corresponding author. Address: Refrigerating Process Engineering Unit, Parc de Tourvoie, Cemagref-BP 44, 92163 Antony cedex, France. Tel.: +33 1 40 96 60 88; fax: +33 1 40 96 62 49.
E-mail address: jean.moureh@cemagref.fr (J. Moureh).

0142-727X/$ - see front matter © 2004 Elsevier Inc. All rights reserved.
doi:10.1016/j.ijheatfluidflow.2004.05.018

Nomenclature

C_p	specific heat of air ($J\,kg^{-1}\,K^{-1}$)
$C's$	turbulence model coefficients
D_H	hydraulic diameter of the inlet section (m)
$f's$	functions to modify the model coefficients
G	production term ($m^2\,s^{-3}$)
H	height of the enclosure (m)
I	turbulence intensity (%)
k	kinetic energy of turbulence ($m^2\,s^{-2}$)
L	length of the enclosure (m)
p	static pressure (Pa)
Re	Reynolds number, $Re = \rho U_0 D_H/\mu$
Re_y	wall Reynolds number, $Re_y = \rho y\sqrt{k}/\mu$
Re_t	turbulence Reynolds number, $Re_t = \rho k^2/\mu\varepsilon$
T, t	mean, fluctuating temperature (K)
$T_{z.i}$, $T_{z.o}$	average temperatures related to V_z (K)
$\overline{u_i u_j}$	Reynolds stresses component ($m^2\,s^{-2}$)
U_i, u_i	mean and fluctuating velocity component in x_i direction ($m\,s^{-1}$)
U, V, W	lateral, vertical and longitudinal mean velocity components ($m\,s^{-1}$)
u, v, w	lateral, vertical and longitudinal fluctuating velocity components ($m\,s^{-1}$)
$\dot{V}_0$	volumetric airflow rate ($m^3\,s^{-1}$)
V_e	enclosure volume (m^3)
V_z	local domain (m^3)
$\dot{V}_z$	volumetric airflow rate supplying V_z ($m^3\,s^{-1}$)
w_0	width of the inlet section (m)
x, y, z	lateral, vertical and longitudinal coordinates (m)
y^+	dimensionless wall unit, $y^+ = (\tau_w/\rho)^{0.5} y/\nu$

Greeks

ε	turbulence energy dissipation rate ($m^2 s^{-3}$)
μ	dynamic viscosity ($kg\,m^{-1}\,s^{-1}$)
ν	kinematic viscosity ($m^2\,s^{-1}$)
ρ	density ($kg\,m^{-3}$)
$\sigma's$	diffusion coefficients in turbulence models
τ_w	wall shear stress ($kg\,m^{-1}\,s^{-2}$)
τ_z	local ventilation efficiency (s^{-1})
τ_0	overall ventilation efficiency (s^{-1})

Subscripts

0	inlet
t	turbulent
i, j, k	vector directions in x, y and z

reported in the literature (Yu and Hoff, 1999; Karimipanah, 1999; Adre and Albright's, 1994; Zhang et al., 2000) consider only short to moderate room lengths ($L/H \leqslant 2.5$, where L is the room length, and H is the room height).

According to the high degree of complexity inherent in the instrumentation of a large enclosure, model studies are practical to characterise airflow behaviour and to validate numerical simulation. Yu and Hoff (1999) investigated the airflow patterns of ceiling slot-ventilated agricultural cold rooms using room models with a two-dimensional wall jet. The authors defined air-jet penetration as the distance from the inlet wall where the wall air-jet separated from the ceiling. They found that the penetration distance was approximately 0.84 times the length of the enclosure ($L = 2.42$ m). In an analogous configuration when the outlet was located on the same wall as the inlet, Adre and Albright's (1994) experiment resulted in a penetration distance of 0.64 L. In addition, the two studies are in agreement concerning the air penetration distance, which varies in a positive manner and remains constant above a threshold Reynolds number value. Threshold values of Re were about 950 for the model and 1900 for the prototype.

Karimipanah (1999) characterized the influence of the opposite end wall on the deflection of wall jets in slot-ventilated enclosures, and recorded pressure distributions along the perimeter of the room for four cases ($L = 2H/3$, H, $4H/3$, and $2H$). According to the pressure behaviour, the author defined the point where the influence of the opposite wall starts as the location where the pressure starts to increase. The region located between this point and the end wall is called the impingement region. The impingement region is located at a point of about 30% of the room length and this holds independently of room size. The pressure level at the corner increases as the room length decreases. However, it is clear that the pressure measurements are unable to explain the behaviour of airflow pattern, especially in the impingement region where the airflow jet is subjected to an adverse pressure gradient. In addition, the influence of the outlet section, located on the same side of the inlet, on the deflection of the jet is not analysed, especially for long room lengths ($L/H > 2.5$).

To improve the design of slot-ventilated enclosures, there is a need to validate numerical models by comparisons with experimental data. After this step, these models should be used to optimize geometric, aerodynamic and thermal parameters. Concerning the use of a turbulence model, many studies use the standard k–ε model described by Launder and Spalding (1974) since it is easy to program and has broad applicability. However,

predictions given by this model tend to be inaccurate and ad-hoc modifications are performed to improve the computed results (see e.g. Choi et al., 1990).

Many authors (Chen and Patel, 1988; Patel et al., 1985; Lam and Bremhorst, 1981) consider that the use of low-Reynolds-number models (LRN) clearly improve the calculations of separated flows over the use of wall functions. Moreover, as a very fine grid distribution is needed in the near-wall region where the viscous sublayer can be resolved, the computing time and memory storage costs are significantly high. These aspects constitute the principal limitation for the LRN models.

Within a confined enclosure, airflow is complicated, since it is often the combination of free turbulent shear flows and near-wall effect. Interactions between airflow and pressure gradient imply the presence of primary and secondary recirculations including high streamline curvature effect. For these complex flows, different authors (Wilcox, 1994; Menter, 1997; Nallasamy, 1987) agree on the inadequacy of k–ε model to predict airflow patterns and underline its limitation by comparison with experimental data. In a comparison concerning indoor air flow Chen (1995) tests five k–ε, two-equation models: the standard k–ε model, a LRN k–ε model, a two-layer k–ε model, a two-scale k–ε model, and a renormalization group (RNG) k–ε model. The author concludes that either of these two-equation models is able to predict the presence of the secondary recirculating flow. Nady et al. (1995) also underline the inability of the k–ε model to predict the detachment of the jet from the ceiling as observed experimentally under non-isothermal conditions.

Gibson and Rodi (1981) show that the standard k–ε model lacks sensitivity to curvature in contrast to the full Reynolds stress model. Leschziner and Rodi (1984) derived after some simplifications the expression of the C_μ coefficient in the Reynolds stress transport equations in curvilinear coordinates. C_μ is not a constant as in the standard k–ε models but depends strongly on streamline curvature. In a comparative review, Nallasamy (1987) concludes that the use of RSM models to account for curvature effects, countergradient transport and secondary flows would improve the confidence in turbulence closure models. For ventilated enclosure, Karimipanah (1999) also recommends the use of second-moment closure turbulence models in order to better predict the appearance of corner flows on the opposite wall where the effect of anisotropy of turbulence fluctuations and streamline curvature are pronounced.

The objective of this study was to numerically and experimentally investigate velocity characteristics throughout a long slot-ventilated enclosure ($L/H \approx 6$) as a function of inlet flow arrangement located on the same side of the exit section. Two configurations with central and lateral air inlet sections were studied. The results concerning airflow characteristics and air-ventilation efficiency were compared and contrasted. Velocity and turbulence measurements were obtained using a scale model under isothermal conditions with laser Doppler velocimetry. Numerical approach was performed using computational fluid dynamics (CFD) Fluent code by testing various turbulence closure models including the high and low Reynolds number form of the two-equation k–ε model, and the more advanced RSM.

The primary focus was to compare the predicted values of velocity and airflow patterns with experimental data obtained using a scale model. In addition, these comparisons allow critical evaluation of the performance of the turbulence models in internal flows. The analysis of experimental and numerical data should identify the mechanisms governing the stability of the confined wall jet on the ceiling or its separation, its reach, the importance of the primary jet zone and in some cases the presence of secondary or recirculating zones.

2. Materials and methods

2.1. Experimental device

The experiments were carried out using a reduced-scale (1:3.3) model of a trailer with respect to the adimensional Reynolds number ($Re = \rho W_0 D_H/\mu$). Afterwards, all the data: dimensions, flow rate and results, are expressed for the actual scale. The blowing and outlet sections are located on the same side at the front of the trailer. The dimensions of this device expressed using the actual scale are represented in Fig. 1. The air is supplied through a rectangular inlet section located near the ceiling, at a relatively high velocity. Due to the Coanda effect, this design should allow to the issuing confined wall jet to adhere, as far as possible, to the ceiling and to entrain the air in the whole enclosure. The objective is to improve the ventilation efficiency and to obtain a nearly uniform distribution of temperature and contaminant through the enclosure.

In this study, two air inlet configurations are studied with central and lateral positions showed respectively in Figs. 1b and c. According to the extensive use of central position for ventilation enclosure, two sections were tested: a small section: $w_0 = 1$ m; which is generally used in the case of refrigerated vehicle configuration and a large section: $w_0 = 2.3$ m. For all these configurations, an inlet airflow rate of 4750 m^3/h was obtained. The opening height was 0.12 m. For the small section, the inlet velocity W_0 is 11 m/s, $D_H = 0.18$ and the kinematic viscosity is 1.5×10^{-5} m^2/s resulting in a Re of 1.3×10^5 in experiments and numerical simulations.

The walls of the scale model are made of wood. Only one lateral wall is made of glass to allow internal air velocity measurement using one-dimensional laser Dop-

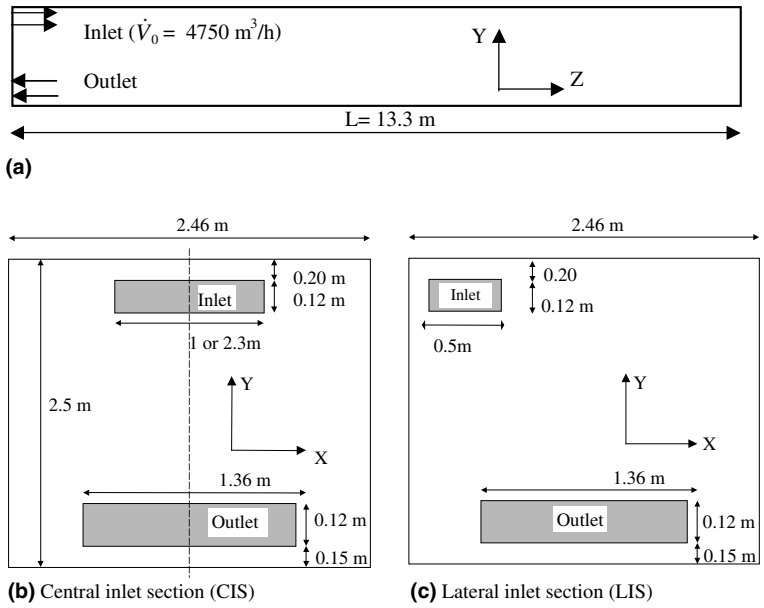

Fig. 1. Schematic view of the slot-ventilated enclosure showing inlet and outlet positions and dimensions: (a) longitudinal view, (b) cross-section of CIS, (c) cross-section of LIS.

pler velocimetry (LDV) produced by TSI manufacturer. This system does not interfere with the flow and is able to correctly resolve the sign as well as the magnitude of velocity and to determine mean velocity and its fluctuation. It comprised a 50 mW laser diode emitting a visible red beam at 690 nm wavelength, a beamsplitter, a Brag cell, a focussing and receiving lens, a pinhole arrangement to collect scattered light and a photomultiplier. Light scattered from particles is captured through the same front lens that the two beams exit from. The air supplied to the model was passed through atomizers and allowed near continuous Doppler signals which were converted into velocity and time. The probe is positioned by a computer controlled traversing arm which provides a resolution of ±0.5 mm in three directions. In these experiments, the decay of the velocity along the enclosure, horizontal and vertical velocity different profiles at different longitudinal positions are obtained. In addition to these profiles, 1080 measurements for horizontal and vertical velocities are performed in the whole medium/symmetry plane in order to represent the streamlines and airflow pattern. The measurement scheme used a uniform grid with 0.5 m horizontal intervals and 0.1 m vertical intervals.

2.2. Analysis of ventilation efficiency

The overall ventilation efficiency is often characterised by the number of times the enclosure's air volume is replaced during one time unit.

$$\tau_0 = \frac{\dot{V}_0}{V_e} \tag{1}$$

An extension of this concept is proposed here in order to characterise the local ventilation efficiency. Thus we analyse the flow rate $\dot{V}_z$ flowing in and out of the volume V_z comprised between z section and the end wall of the enclosure, as shown in Fig. 2a. According to numerical simulations, $\dot{V}_z$ can be computed by the following integration:

$$\dot{V}_z = 0.5 \int_{S_z} |W| \, \mathrm{d}s \tag{2}$$

However, the air flowing in the volume V_z is not only composed of fresh injected air but also by recirculating air (Fig. 2b). If ventilation is used to extract heat or an undesirable gaseous component which is generated in the enclosure, only the fresh injected air is efficient. In order to characterize the quantity of fresh air part entering the volume V_z, a fictitious and uniform volumic heat load per unit volume, P, is applied throughout the enclosure domain.

In steady state, the heat balance of the control volume V_z can be expressed using bulk average air temperatures of the air flowing in and out, named $T_{z.\mathrm{i}}$ and $T_{z.\mathrm{o}}$ respectively.

$$PV_z = \dot{V}_z \rho C_p (T_{z.\mathrm{o}} - T_{z.\mathrm{i}}) \tag{3}$$

Moreover, the incoming airflow can be considered as the mixing of a quantity of fresh air named $\dot{V}_{z.\mathrm{eq}}$ at temperature T_0 and a recirculating air $(\dot{V} - \dot{V}_{z.\mathrm{eq}})$ at temperature $T_{z.\mathrm{o}}$ (Fig. 2b).

$$\rho C_p \dot{V}_z T_{z.\mathrm{i}} = \rho C_p \dot{V}_{z.\mathrm{eq}} T_0 + \rho C_p (\dot{V}_z - \dot{V}_{z.\mathrm{eq}}) T_{z.\mathrm{o}} \tag{4}$$

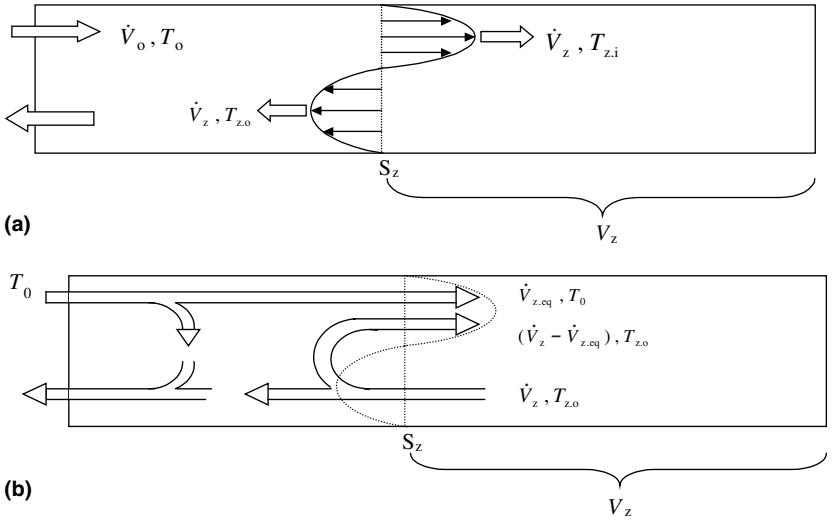

Fig. 2. Local ventilation concerning V_z domain: (a) schematic view of the flow rate $\dot{V}_z$ supplying V_z domain through z section, (b) schematic decomposition of $\dot{V}_z$ between fresh air $\dot{V}_{z.eq}$ and recirculating air $(\dot{V}_z - \dot{V}_{z.eq})$.

Thus the heat balance can be rewritten:

$$PV_z = \rho C_p \dot{V}_{z.eq}(T_{z.o} - T_0) \tag{5}$$

This means that, in terms of heat extraction capacity (or gaseous component extraction), the process gives rise to an equivalent flow rate of fresh injected air $\dot{V}_{z.eq}$ entering the volume V_z. The additional airflow part: $\dot{V}_z - \dot{V}_{z.eq}$ flows in a circular manner, and contributes to the uniformity of temperature in the V_z domain; however, it does not affect the heat balance.

Thus the bulk temperatures, $T_{z.i}$ and $T_{z.o}$ can be computed from the simulations by following integration:

$$\dot{V}_z T_{z.i} = 0.5 \int_{S_z} (|W| + W) T \, ds \tag{6a}$$

$$\dot{V}_z T_{z.o} = 0.5 \int_{S_z} (|W| - W) T \, ds \tag{6b}$$

Then $\dot{V}_{z.eq}$ can be obtained from Eq. (4). Finally, we define a local ventilation efficiency based on the equivalent fresh air renewal:

$$\tau_z = \frac{\dot{V}_{z.eq}}{V_z} \tag{7}$$

3. Numerical modelling

3.1. Governing equations and hypothesis

The description of airflow development are based on the conservative law of mass and momentum. The solved equations can be written as follows:

Mass conservation:

$$\frac{\partial U_j}{\partial x_j} = 0 \tag{8}$$

Momentum conservation:

$$\frac{\partial U_j U_i}{\partial x_j} = -\frac{1}{\rho}\frac{\partial P}{\partial x_i} + \frac{\partial}{\partial x_j}\left(\nu \frac{\partial U_i}{\partial x_j} - \overline{u_i u_j}\right) \tag{9}$$

Energy conservation:

$$\frac{\partial U_j T}{\partial x_j} = \frac{\partial}{\partial x_j}\left(\frac{\nu}{Pr}\frac{\partial T}{\partial x_j} - \overline{u_j t}\right) \tag{10}$$

where $\overline{u_i u_j}$ and $\overline{u_j t}$ are, respectively, the unknown Reynolds stresses and heat fluxes. The obtaining of these quantities depends on the turbulence closure. For the case investigated, two levels of turbulence modelling closure have been employed:

- on one hand with two-equation models: the high and low Reynolds number form of the two-equation k–ε model, based on the Boussinesq hypothesis.
- on the other hand with a second-moment closure.

3.1.1. The standard k–ε model: high–Reynolds number

Using the Boussinesq hypothesis, the Reynolds stresses can be described as follows:

$$-\overline{u_i u_j} = \nu_t\left(\frac{\partial U_i}{\partial x_j} + \frac{\partial U_j}{\partial x_i}\right) - \frac{2}{3}k\delta_{ij} \tag{11}$$

the eddy (turbulent) viscosity ν_t is obtained from:

$$\nu_t = C_\mu f_\mu \frac{k^2}{\varepsilon} \tag{12}$$

The turbulence kinetic energy k and the dissipation rate ε are determined using the following transport equations respectively:

$$\frac{\partial U_j k}{\partial x_j} = \frac{\partial}{\partial x_j}\left[\left(\nu + \frac{\nu_t}{\sigma_k}\right)\frac{\partial k}{\partial x_j}\right] + G_k - \epsilon \tag{13}$$

$$\frac{\partial U_j \epsilon}{\partial x_j} = \frac{\partial}{\partial x_j}\left[\left(\nu + \frac{\nu_t}{\sigma_\epsilon}\right)\frac{\partial \epsilon}{\partial x_j}\right] + \frac{\epsilon}{k}(C_1 f_1 G_k - C_2 f_2 \epsilon) \quad (14)$$

G_k represents the shear production term:

$$G_k = \nu_t\left[\frac{\partial U_i}{\partial x_j} + \frac{\partial U_j}{\partial x_i}\right]\frac{\partial U_i}{\partial x_j} \quad (15)$$

With the exception of the low-Reynolds number k–ε models, the damping functions f_μ, f_1, f_2 are equal to one.

The model coefficients in the standard k–ε model are:

$$(C_\mu, C_1, C_2, \sigma_k, \sigma_\varepsilon) = (0.09, 1.44, 1.92, 1.0, 1.3) \quad (16)$$

3.1.2. The Lam–Bremhorst model: low-Reynolds number k–ε

In regions very near a wall where viscous effects become important, properties will change rapidly, the damping functions proposed by the Lam–Bremhorst model (1981) are equal to:

$$f_\mu = [1 - \exp(-0.0165 Re_y)]^2(1 + 20.5/Re_t) \quad (17)$$

$$f_1 = 1 + (0.05/f_\mu)^3 \quad (18)$$

$$f_2 = 1 - \exp(-Re_t^2) \quad (19)$$

The definitions of the Reynolds number used in these formulae are:

$$Re_y = \rho y\sqrt{k}/\mu \quad (20)$$

$$Re_t = \rho k^2/\mu\varepsilon \quad (21)$$

3.1.3. The RSM

To obtain the transport equations for Reynolds turbulent stress we multiply the i-component Navier–Stokes equation for the instantaneous velocity $(U_i + u_i)$ by the fluctuation u_j. We then add u_i times the equations for $(U_j + u_j)$, and average. This gives rise to:

$$U_k\frac{\partial \overline{u_i u_j}}{\partial x_k} = -\frac{\partial}{\partial x_k}\left[\overline{u_i u_j u_k} + \frac{p}{q}(\delta_{kj}u_i + \delta_{ik}u_j) - \nu\frac{\partial(\overline{u_i u_j})}{\partial x_k}\right] + G_{ij} + \overline{\frac{p}{q}\left[\frac{\partial u_i}{\partial x_j} + \frac{\partial u_j}{\partial x_i}\right]} - 2\nu\overline{\frac{\partial u_i}{\partial x_k}\frac{\partial u_j}{\partial x_k}} \quad (22)$$

where $G_{ij} = -\overline{u_i u_k}\frac{\partial U_j}{\partial x_k} - \overline{u_j u_k}\frac{\partial U_i}{\partial x_k}$ represents the production term.

The diffusive transport term was represented by a simplified form of the generalized gradient diffusion hypothesis as

$$-\frac{\partial}{\partial x_k}\left[\overline{u_i u_j u_k} + \frac{p}{\rho}(\delta_{kj}u_i + \delta_{ik}u_j) - \nu\frac{\partial(\overline{u_i u_j})}{\partial x_k}\right] = \frac{\partial}{\partial x_k}\left(\frac{\nu_t}{\sigma_k}\frac{\partial}{\partial x_k}(\overline{u_i u_j})\right) \quad (23)$$

The pressure–strain term consisted of the linear return-to-isotropy and is modelled by Launder et al. (1975) as

$$\overline{\frac{p}{\rho}\left[\frac{\partial u_i}{\partial xj} + \frac{\partial u_j}{\partial xi}\right]} = -C_1\frac{\epsilon}{k}\left[\overline{u_i u_j} - \frac{2}{3}\delta_{ij}k\right] - C_2\left[G_{ij} - \frac{2}{3}\delta_{ij}G\right] \quad (24)$$

where the constants $C_1 = 1.8$ and $C_2 = 0.60$, and $G = 0.5G_{ii}$.

The dissipation term was assumed isotropic, and was approximated by

$$2\nu\overline{\frac{\partial u_i}{\partial x_k}\frac{\partial u_j}{\partial x_k}} = \frac{2}{3}\delta_{ij}\varepsilon$$

where the dissipation rate was computed via the ε transport equation.

The turbulent heat fluxes was expressed as

$$\overline{u_j t} = -\frac{\nu_t}{Pr_t}\frac{\partial T}{\partial x_j} \quad (25)$$

3.2. Boundary conditions

The computational domain may be surrounded by inflow and outflow boundaries in addition to symmetry and solid walls. At the inlet, uniform distribution is assumed for velocity components, kinetic energy of turbulence (k_0) and the energy dissipation rate (ε_0). The numerical values are specified as

- $U_0 = V_0 = 0$; $W_0 = 11$ m/s representing the mean streamwise longitudinal velocity, giving an inlet flow rate $\dot{V}_0 = 4750$ m^3/h,
- $k_0 = 3/2(U_0 I_{0z})^2$; where $I_{0z} = 10\%$ represents the turbulence intensity of the z-component of velocity at the inlet as obtained from experiments,
- $\varepsilon_0 = (C_\mu^{0.75}k_0^{1.5}/0.07D_H)$ where D_H represents the hydraulic diameter of the inlet section,
- for the RSM, turbulence is assumed to be isotropic: $\overline{u_i u_j} = \frac{2}{3}k_0\delta_{ij}$.

At the outflow, pressure is supposed to be uniform and zero-gradient is applied for all transport variables.

Excepting the case of LRN, the turbulence models are only valid in fully turbulent regions. Close to the wall, where viscous effects become dominant, these models are used in conjunction with wall functions. For this study, the conventional equilibrium logarithmic law governing the wall is used (Launder and Spalding, 1974).

At the symmetry plane, only valid for CIS configuration, zero normal velocity and zero normal gradients of all variables are assigned.

Table 1
Various grid densities used in numerical simulations

Model	Grid: $N_x \cdot N_y \cdot N_z$ in depth (2.46 m), height (2.5 m) and length (13.3 m)	
	Coarse	Fine
k–ε (standard)		$50 \times 52 \times 240$
LRN k–ε		$60 \times 87 \times 124$
RSM	$47 \times 48 \times 151$	$50 \times 52 \times 240$

3.3. Numerical resolution

The computations were carried out using FLUENT, a commercial computational fluid dynamics (CFD) code with a three-dimensional configuration. The governing equations are solved using the finite-volume method in a staggered grid system. In these simulations, the quick scheme, based upon three-point upstream-weighted quadratic interpolation as described by Leonard (1979) was used rather than linear interpolation between consecutive grid points. The principal objective in using the quick scheme is to reduce the grid size required to yield a grid-independent solution, in comparison to the low-order scheme.

A non-uniform grid was used in this study, with high-density mesh in regions near the inlet, outlet and walls where high gradients are expected. The different grids used are presented in Table 1. The results presented here are for the finer grid for both LIS and CIS. Using the symmetry assumption, only half of the enclosure is simulated in CIS.

4. Results and discussion

4.1. General description of the flow field

4.1.1. Central inlet configuration (CIS)

In order to better understand the behaviour of the flow patterns within the enclosure, we represent in Fig. 3a the streamlines related to the mean flow field in the symmetry plane. These streamlines are obtained from 1080 (24×45) measurement points made using the LDV system. On the same plane, Fig. 4a presents the decrease in the velocity for normal and large inlet sections. It can be seen that the wall jet separates from the ceiling at approximately $z/L = 8.5/13.3$ and $7/13.3$ from the inlet respectively for normal and large sections. This separation splits the jet into two regions dominated by two vortices of opposite circulation. The primary recirculation located in the front part of the enclosure delimits the reach and the action of the inlet jet. Conversely,

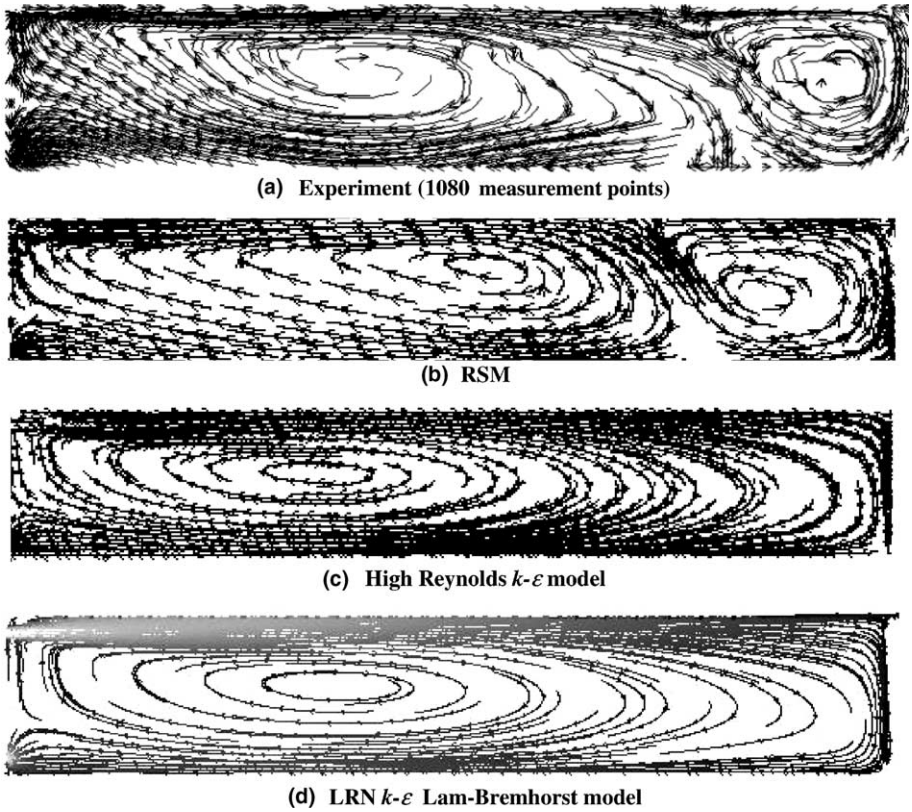

Fig. 3. Airflow pattern on the symmetry plane: comparisons between experiment and numerical results.

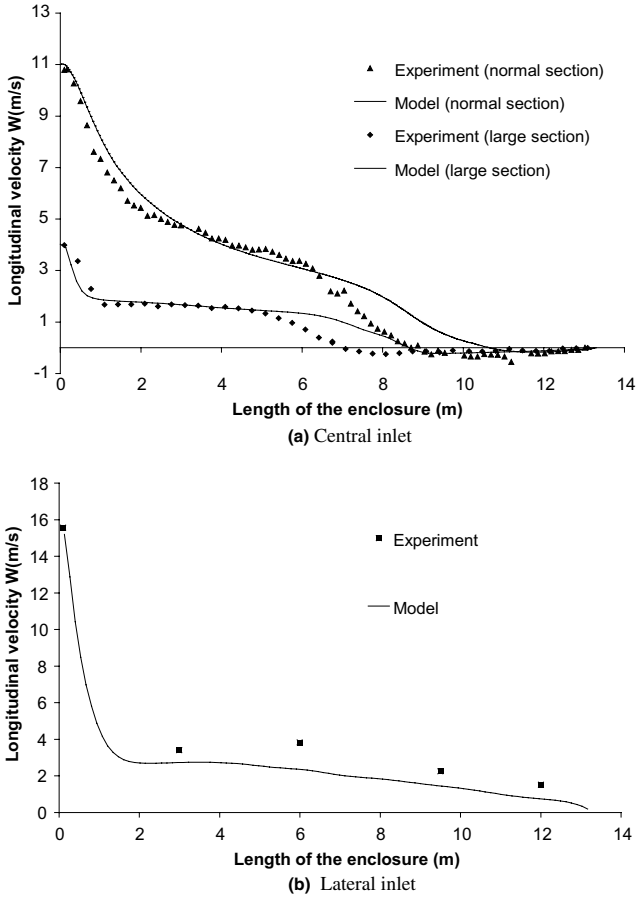

Fig. 4. Decay of the jet velocity along the enclosure: comparisons between experiment and numerical results (RSM fine grid): (a) CIS for normal and large section, (b) LIS.

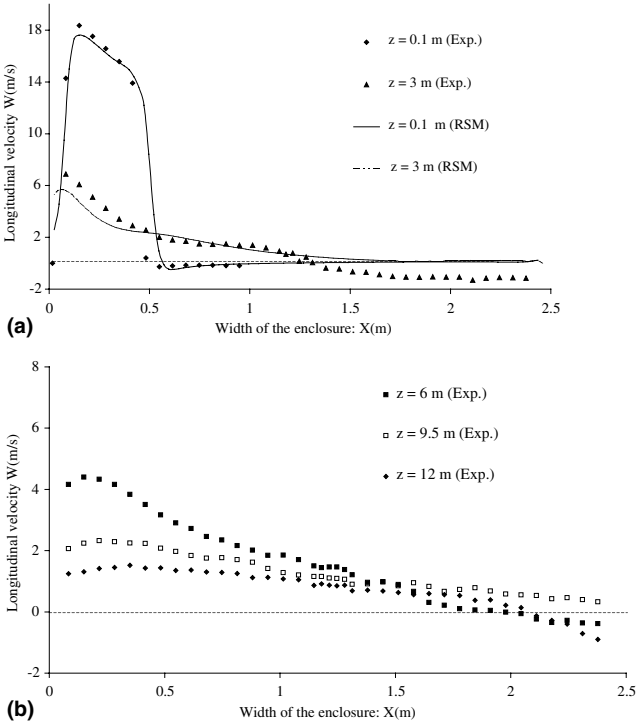

Fig. 5. Horizontal velocities for LIS: (a) $z = 0.1$ and 3 m: comparisons between experiment and numerical results; (b) $z = 6$, 9.5 and 12 m: experimental data.

the secondary flow located in the rear part is poorly supplied by the primary jet. In addition, the velocities are very low. This type of airflow is highly undesirable because of the stagnant zone aspect related to the secondary recirculating area where high levels of temperature and contaminant could be expected due to the poor mixing with the primary recirculating air.

4.1.2. Lateral inlet configuration (LIS)

In comparison with CIS, LIS is designed in order to improve the homogeneity of airflow distribution and ventilation efficiency in the whole enclosure. From an aerodynamic standpoint, the aim is to avoid the separation of the wall jet and hence the appearance in the rear end of the enclosure of a secondary recirculation dominated by low velocities.

Fig. 4b shows the decrease in the velocity from the middle of the blowing section. It can be seen that the wall jet does not separate from the wall and reaches the opposite side of the enclosure. This trend can also be confirmed by horizontal profiles obtained at 0.1, 3, 6, 9.5 and 12 m (Fig. 5).

4.2. Wall jet separation analysis

Airflow pattern and velocity characteristics in an enclosure have some original features which can be highlighted. In the case of an unbounded wall jet, the maintaining of the jet on the wall can be easily explained by the Coanda effect. In the enclosure, the maintenance of the jet at ceiling level is more complex because it involves the action of the pressure gradient in horizontal and vertical directions.

In order to illustrate the Coanda effect on the jet behaviour at the inlet, Fig. 6 shows the vertical position of higher horizontal velocities of the jet along the blowing axis for a CIS. As expected, numerical and experimental data confirm that the jet moved towards the ceiling, which it reached it at approximately 3 m, and flowed along it until its separation.

Just after the inlet, the flow has the distinctive characteristics of a jet. It expands with an angle of about 10° and entrains the surrounding fluid. Between the inlet ($z = 0$) and up to $z = 4$ m, the airflow rate increased (Fig. 7) and the jet decay of the maximum velocity of the jet is similar to an unbounded 3D wall jet (Zertal-Ménia, 2001) as can be estimated from standard expression given by Viets and Sforza (1966). Further downstream, the jet decreases faster than an unbounded wall jet until its separation. Within the enclosure, the development of the wall jet is limited by the effect of

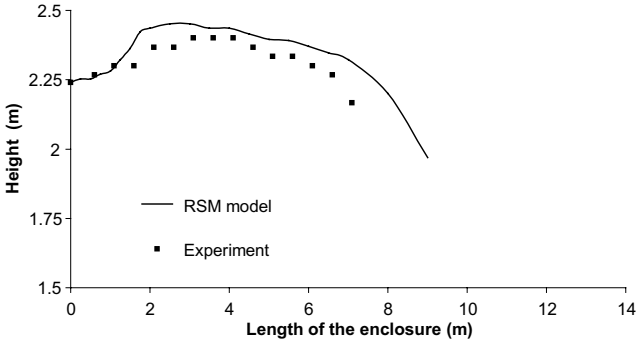

Fig. 6. Vertical positions of higher horizontal velocities along the blowing axis: comparison between experiment and numerical results (CIS, normal section).

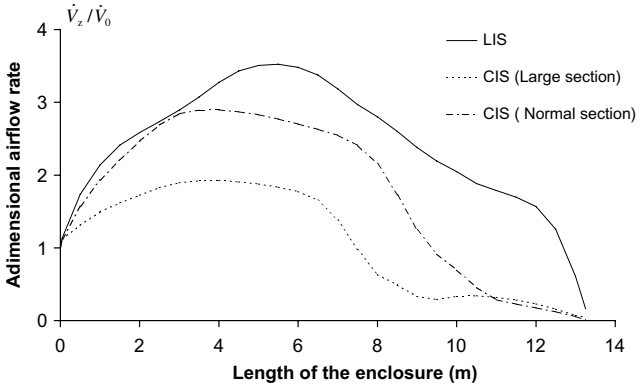

Fig. 7. Evolution of the adimensional airflow rate $\dot{V}_z/\dot{V}_0$ through the enclosure: RSM.

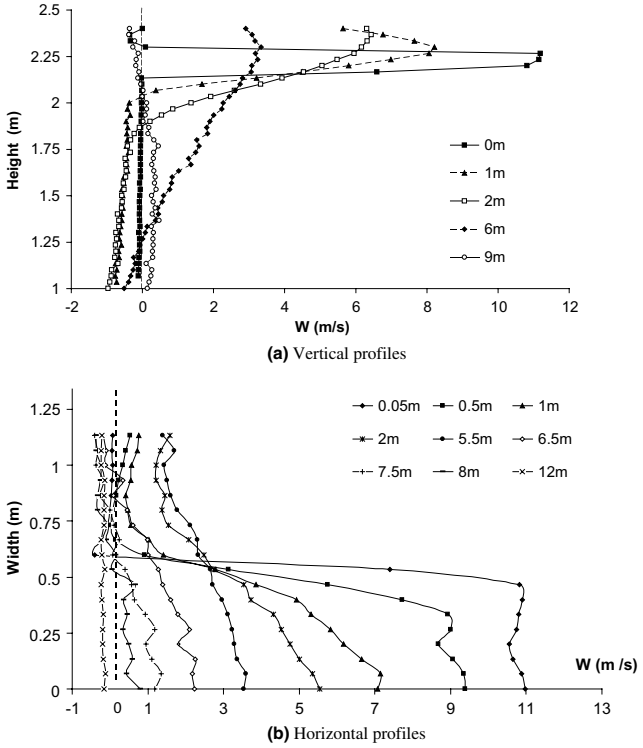

Fig. 8. Experimental longitudinal velocity component (W) velocity profiles for CIS: (a) vertical profiles along the medium plane at 0, 1, 2, 6 and 9 m, (b) horizontal profiles in the middle of the inlet section at 0.05, 0.5, 1, 2, 5.5, 6.5, 7.5, 8 and 12 m.

both lateral and vertical confinement due respectively to the interaction of the mean flow with the lateral enclosure wall, which probably begins at 4 m, and with reverse flow in the direction of the outlet as shown in vertical velocity profiles (Fig. 8a). This confinement effect reduces the entrainment of the jet with its surroundings and leads to stabilisation of the airflow rate at a distance of approximately 4–6 m from the inlet (Fig. 7).

The principle difference with an unbounded case can be explained by the effect of both lateral and vertical confinement due respectively to the interaction of the mean flow with the lateral enclosure wall which probably begins at 4 m and with the reverse flow flowing towards the outlet as shown in vertical velocity profiles (Fig. 8a). This confinement effect reduces the entrainment of the jet with its surroundings and causes the stabilisation of airflow rate (Fig. 7).

Owing to the airflow rate stabilisation, the mixing process causes the velocity profile to flatten with distance (Fig. 8b) and in turn implies the decreasing of the total flux of momentum. This decay can only be compensated for by an adverse pressure gradient which is observed between 7 and 9 m (data not shown). In addition, the presence of the reverse flow due to the vertical confinement prevents the pressure from being vertically uniform and causes a normal vertical pressure gradient, acting against the Coanda effect, to arise. The cumulative action of these two adverse pressure gradients can obviously explain the separation of the wall jet which occurs at 8.5 m. Consequently, a stagnant zone with low velocities and a quasi-uniform pressure is present at the rear between the end wall and the zone of separation.

As shown in Fig. 4a, the use of a large section decreases the reach of the jet and hence increases the secondary recirculation area: the separation point varies from approximately 8.5 m for a normal section to 7 m for a large section. This aspect underlined the importance of the confinement effect which became more pronounced with a large section because the interaction between the flow and the lateral walls enclosure begins almost immediately after the inlet.

In LIS, although the jet decay near the inlet is faster than that of CIS (Fig. 4), positives values of longitudinal velocity are maintained in the jet even in the rear part as can be observed on horizontal profiles (Fig. 5). Obviously, LIS design in which the jet is flowing in a corner bounded by two walls, reinforces the Coanda effect, avoids the separation of the wall jet and maintains it

on the ceiling along the enclosure. In addition, secondary motions in the corner of the enclosure (not shown here), help keep the jet attached. Consequently, the formation of a stagnant zone in the rear is avoided and ventilation is more homogeneous throughout the entire enclosure.

4.3. Turbulence modelling performance

The comparisons concerning streamlines behaviour (Fig. 3) show that only RSM is able to predict correctly the separation of the wall jet and the general behaviour of air motion related to the primary and to the secondary recirculations. The same figure also shows the poor predictions given by the k–ε turbulence model, and underlines its inability to predict flow separation. Results obtained using the LRN k–ε model (Fig. 3d) and the other two-equation turbulence models, RNG and k–ω (not presented here) are similar to those obtained with the k–ε model.

To check grid non-dependence, other simulations were performed by Zertal-Ménia (2001) with the RSM. Comparisons (not presented here) show that the coarse grid of $47 \times 48 \times 151$ cells leads to an inaccurate solution, probably due to the predominance of numerical diffusion.

In addition to the presence of the adverse pressure gradient in the area preceding the separation of the wall jet, Fig. 9 shows also a high degree of anisotropy between two normal components of Reynolds stresses: $\overline{v^2}$ and $\overline{w^2}$ obtained experimentally in the same area. All these aspects justify the use of the second moment closure instead of the two-equation turbulence models in order to better predict the complexity of the flow in the separation region where the effect of anisotropy of turbulence fluctuations and streamline curvature are pronounced. Due to marked variations in velocity along the enclosure, the y^+ quantity related to the adjacent first cell (RSM data not shown) varies from 220 near the blowing inlet to 10 at the rear of the vehicle. Concerning LRN k–ε model, y^+ wall values vary from 2.8 to 0.1. Consequently, there is a need to perform another LRN k–ε simulations with more refined grids to obtain y^+ values close to 1 and to reduce the aspect ratio of cells located near the ceiling. This step actually allows to check the ability of this model in detecting the separation of the wall jet.

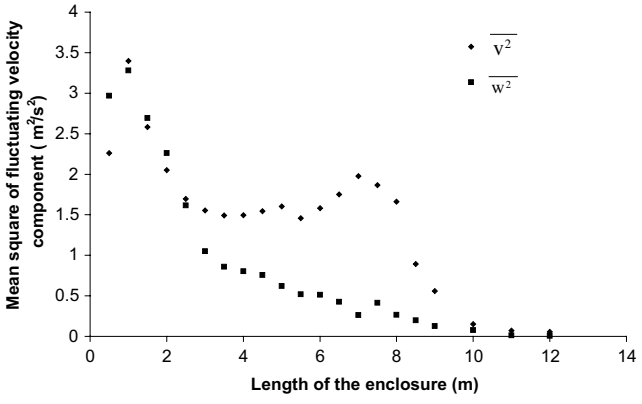

Fig. 9. Evolution of $(\overline{v^2})$ and $(\overline{w^2})$ along the blowing axis (at 0.26 m from the wall) for CIS: experimental data.

This failure of the k–ε based models in predicting complex flows, including secondary and/or separated flows caused by adverse pressure gradient, was observed by many authors. According to Wilcox (1994) and Menter (1997), the k–ε model predicts significantly too high shear-stress levels and thereby delays or completely prevents separation. According to Launder (1992), this trend can be more pronounced in the presence of adverse pressure gradient and leads to overprediction of the wall shear stress. We believe that this implies the non-separation of the jet from the ceiling and leads to increased domination of the primary recirculation in the whole enclosure.

The good prediction of the RSM model are also observed for the vertical velocity profile at 1 and 3 m (Fig. 10). On the same figure, the slight difference concerning the 6 m profile can be explained by the position of the centre of the primary recirculation, which is predicted more downstream in the RSM: 7 m instead 5 m according to experiments. Consequently, predicted maximal velocity positions for the 6 m profile are closer to the ceiling than experimental data.

In the case of CIS, comparisons between numerical and experimental data also show that the RSM model become less accurate near the point of the detachment of the jet (Figs. 4a and 10c). According to LDV measurements, these differences can be explained by the instability of the detachment point position and by the non-stationary character of velocities in this area. From a numerical standpoint, a better analysis taking into account the spatial–temporal character of these fluctuations necessitates the use of more advanced non-stationary approaches such as large eddy or direct numerical simulations instead of averaged turbulence models. However, the drawbacks in terms of computing cost and memory storage could be too high, especially for this large domain.

Fig. 11 shows comparisons between numerical and experimental data concerning the evolution of the mean-square of the fluctuating velocity in the z direction $(\overline{w^2})$ along the blowing axis. Both curves have two peaks. The first peak is a common characteristic of turbulent jet expansion due to diffusion of the turbulence from the edge to the core of the jet. The second peak located near the area of separation of the jet from the wall reflects the extra amount of turbulence generated in this region where high gradients of velocities were locally present.

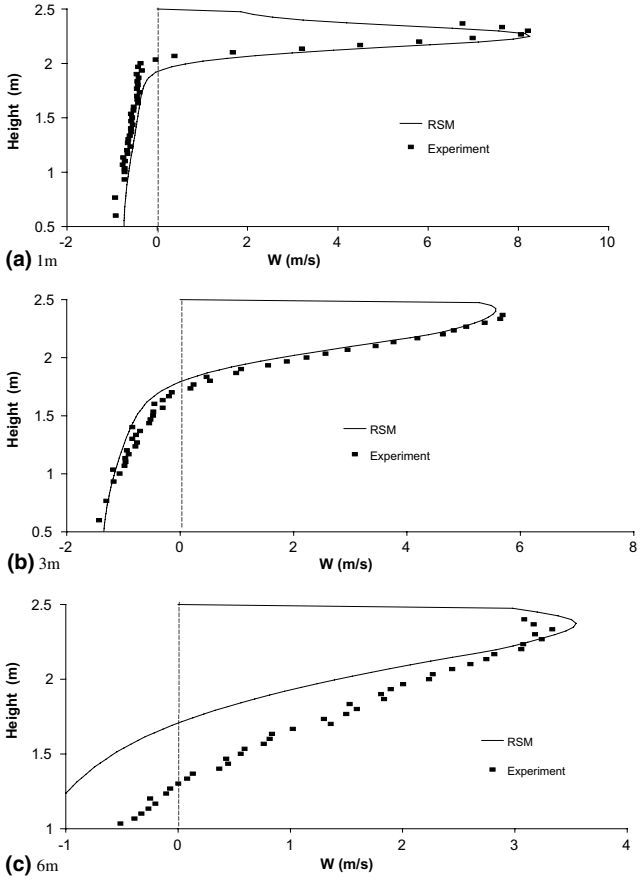

Fig. 10. Vertical profiles of longitudinal velocities along the medium plane at 1, 3 and 6 m: comparisons between experiment and numerical results.

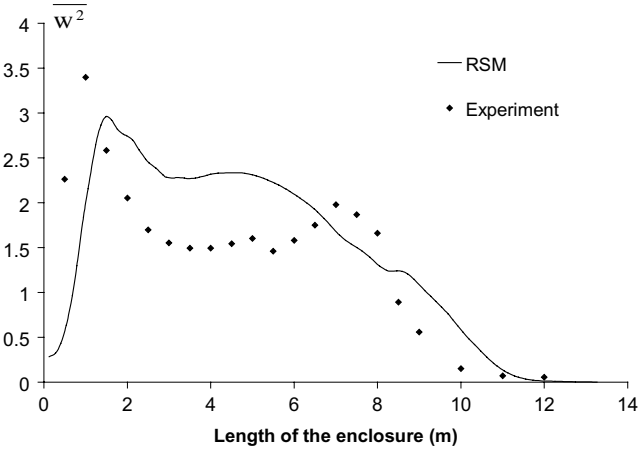

Fig. 11. Evolution of the mean-square of the longitudinal fluctuating velocity ($\overline{w^2}$) along the blowing axis for CIS: comparison between experiment and numerical results.

Fig. 12 shows the longitudinal evolution of the wall shear stress ($\tau_w = \overline{vw}$) along the ceiling of the enclosure. The first local peak located at $z = 1$ m coincides with the point where the jet reaches and attaches itself to the ceiling. The maximum $\overline{vw}$ values are reached at $z = 4$ m which corresponds approximately to the centre of the primary recirculation, which reinforces the Coanda effect.

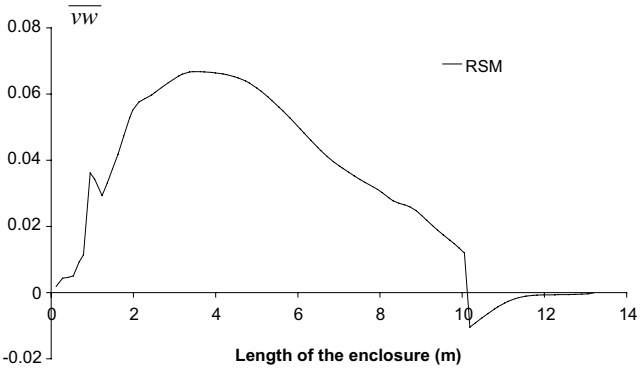

Fig. 12. Evolution of the wall shear stress ($\overline{vw}$) along the ceiling for CIS: RSM.

Downwards, the increasing action of the adverse pressure underlined above leads to diminishing wall shear stress values until the separation of the jet around 9 m. At the separation point, the wall shear stress and y^+ vanish and show slight discontinuity. In addition, $\overline{vw}$ changes the sign, corresponding to inverse recirculation of flow on each side of the separation point. However, we should note that at this point, the logarithmic law of the wall is not valid.

4.4. Analysis of ventilation efficiency

Figs. 7 and 13 represent respectively a comparison between CIS and LIS concerning the evolution of $\dot{V}_z/\dot{V}_0$ and τ_z/τ_0 along the enclosure. The results lead us to the following remarks:

- Fig. 7 shows that all configurations present the same behaviour of adimensional airflow rate $\dot{V}_z/\dot{V}_0$ along the enclosure from the inlet to the opposite end. Due to the entrainment by the wall jet, the airflow rate is increased from the inlet until the centre of recirculation where maximum values of $\dot{V}_z/\dot{V}_0$ are reached. The maximum values are 3.5 for LIS, 2.9 for CIS (normal section) and 1.9 for CIS (large section) and they are reached at 5.5, 3.5 and 3.5 m respectively. The highest value for LIS can be explained by the asymmetrical design between inlet and outlet which allow better occupancy of the enclosure by primary and reverse flow.
- As it can be seen on Fig. 13, $\tau_z = \frac{\dot{V}_{z,eq}}{\dot{V}_z}$ values for CIS and LIS are similar and higher than the overall value $\tau_0 = \frac{\dot{V}_0}{\dot{V}_e}$ up to 7 m from the inlet. This reflects high and adequate ventilation efficiency in this zone dominated by primary recirculating for CIS. Conversely, in the rear part of the enclosure, the behaviour of τ_z differs

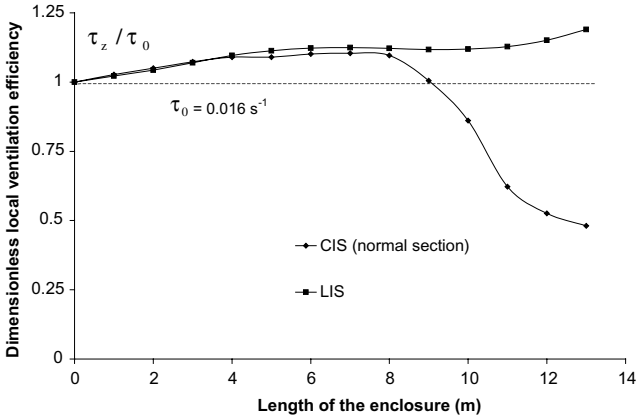

Fig. 13. Evolution of the dimensionless local ventilation efficiency τ_z/τ_0 along the enclosure: RSM.

totally in the two configurations. LIS conserves the uniformity of τ_z values even in the rear part. This can be explained by the non-separation of the wall jet in LIS which avoids the presence of stagnant zones. Consequently, the uniformity of the ventilation is maintained throughout the enclosure. Conversely, for CIS, the τ_z values fall to half the overall value. This reflects low ventilation efficiency and the presence of stagnant zones downwards the separation of the wall jet. Consequently, the simple use of $\tau_0 = \frac{\dot{V}_0}{V_e}$ as a overall ventilation criterion for the whole enclosure leads to underestimation of needs in terms or air renewal requirements in this zone where higher temperature, concentration or pollutant values could be expected.

- These results show that the main advantage of LIS over CIS lies in its capacity to the maintain highest value of $\dot{V}_z/\dot{V}_0$ and the uniformity of τ_z even in the rear part of the enclosure. However, according to numerical results (Fig. 5), LIS produces a moderate stagnant flow region in the corner located opposite the inlet section in the front part of the enclosure.

5. Conclusion

In this study, experiments and numerical simulations were carried out in order to characterize velocities and airflow patterns within a long and empty slot-ventilated enclosure characterized by the presence of inlet and outlet sections on the same side at the front. In addition to the most commonly used central inlet configuration (CIS), an original design with a lateral inlet section (LIS) was also investigated.

In the case of the central inlet section, this study illustrates the effect of confinement on the jet behaviour, its separation and hence the formation of stagnant zones in the rear part of the enclosure. This study also shows that the use of a lateral inlet section reinforces the Coanda effect and avoids separation of the jet. This aspect improves the homogeneity of the ventilation and allows better maintenance throughout the enclosure of the level and the uniformity of indoor ambience parameters such as temperature, concentration and pollutants.

To analyse the uniformity of ventilation efficiency, an original approach is proposed in terms of local ventilation efficiency τ_z. For CIS, τ_z values fall to half the overall value in the rear part of the enclosure. This reflects low ventilation efficiency and the presence of stagnant zones. Conversely, LIS conserves the uniformity of τ_z throughout the enclosure.

The experimental results show the complexity of the confined turbulent flow generated by the wall jet where adverse pressure gradients are present and the effect of anisotropy of turbulence fluctuations and streamline curvature are pronounced. All these aspects justify the use of the second moment closure instead of the two-equation turbulence models in order to be able to predict airflow patterns and flow separation.

References

Adre, N., Albright, L.D., 1994. Criterion for establishing similar air flow patterns (isothermal) in slotted-inlet ventilated enclosures. Transactions of the ASAE 37, 235–250.

Awbi, H.B., 1989. Application of computational fluid dynamics in room ventilation. Building and Environment 24, 73–84.

Chen, H.C., Patel, V.C., 1988. Near wall-turbulence models for complex flows including separation. AIAA Journal 26, 641–648.

Chen, Q., 1995. Comparison of different k–ε models for indoor air flow computations. Numerical Heat Transfer, Part B, 353–369.

Choi, H.L., Albright, L.D., Timmons, M.B., 1990. An application of the k–ε turbulence model to predict how a rectangular obstacle in a slot-ventilated enclosure affects air flow. Transactions in Agriculture 33 (1), 274–281.

Davidson, L., 1989. Ventilation by displacement in a three-dimensional room: a numerical study. Building and Environment 24, 263–272.

Gibson, M.M., Rodi, W., 1981. A Reynolds-stress closure model of turbulence applied to the calculation of a highly curved mixing layer. Journal of Fluid Mechanics 103, 161–182.

Hoff, S.J., Janni, K.A., Jacobson, L.D., 1992. Three-dimensional buoyant turbulent flows in a scaled model, slot-ventilated, livestock confinement facility. American Society of Agricultural Engineers 35, 671–686.

Karimipanah, M.T., 1999. Deflection of wall jets in ventilated enclosures described by pressure distribution. Building and Environment 34, 329–333.

Lam, C.K.G., Bremhorst, K., 1981. A modified form of the k–ε model for predicting wall turbulence. ASME Journal of Fluids Engineering 103, 456–460.

Launder, B.E., 1992. On the modeling of turbulent industrial flows. In: Hirsch, V. et al. (Eds.), Proceedings of computational methods in applied sciences. Elsevier, pp. 91–102.

Launder, B.E., Reece, G.J., Rodi, W., 1975. Progress in the development of a Reynolds stress turbulence closure. Journal of Fluid Mechanics 68, 537–566.

Launder, B.E., Spalding, D.B., 1974. The numerical computation of turbulent flows. Computer Methods in Applied Mechanics and Energy 3, 269–289.

Leonard, B.P., 1979. A stable and accurate convective modeling procedure based on quadratic upstream interpolation. Computer Methods in Applied Mechanics and Energy 19, 59–98.

Leschziner, M.A., Rodi, W., 1984. Computation of strongly swirling axisymmetric free jets. AIAA Journal 22, 1742–1747.

Menter, F.R., 1997. Eddy viscosity transport equations and their relation to the k–ε model. ASME Journal of Fluids Engineering 119, 876–884.

Nady, A., Saïd, M., Shaw, C.Y., Zhang Jianshung, S., Christianson Leslie, L., 1995. Computation of room air distribution. ASHRAE Transactions: Symposia 101, 1065–1077.

Nallasamy, M., 1987. Turbulence models and their applications to the prediction of internal flows: a review. Computers and Fluids, 151–194.

Nielsen, P.V., Restivo, A., Whitelaw, J.H., 1978. The velocity characteristics of ventilated rooms. Journal of Fluids Engineering, 291–298.

Patel, V.C., Rodi, W., Scheuerer, G., 1985. Turbulence model for near-wall and low Reynolds number flows: a review. AIAA Journal 23, 1308–1319.

Viets, H., Sforza, 1966. An experimental investigation of a turbulent wall jet. Rep. 968, Department of Aerospace Engineering, Polytechnic Institute of Brooklyn, New York.

Wilcox, D.C., 1994. Turbulence modeling for C.F.D. DCW Industries, Inc., La cañada, California.

Yu, H., Hoff, S.J., 1999. Airflow pattern criteria for ceiling slot-ventilated agricultural enclosures under isothermal conditions. American Society of Agricultural Engineers 42, 459–469.

Zertal-Ménia, N., 2001. Etude numérique et expérimentale de l'aéraulique dans un véhicule frigorifique, Thèse INA-PG.

Zhang, G., Morsing, S., Bjerg, B., Svidt, K., Strom, J.S., 2000. Test room for validation of airflow patterns estimated by computational fluid dynamics. Journal of Agricultural Engineering Research 76, 141–148.